Engineering 19 (2022) 71–83

Contents lists available at ScienceDirect

Engineering

journal homepage: www.elsevier.com/locate/eng

Research
Air Pollution Control—Article

Ground-Based Hyperspectral Stereoscopic Remote Sensing Network: A Promising Strategy to Learn Coordinated Control of O_3 and $PM_{2.5}$ over China

Cheng Liu [a,b,c,d,e], Chengzhi Xing [c,*], Qihou Hu [c], Qihua Li [h], Haoran Liu [h], Qianqian Hong [i], Wei Tan [c], Xiangguang Ji [c,g], Hua Lin [c,g], Chuan Lu [c], Jinan Lin [c], Hanyang Liu [f], Shaocong Wei [a], Jian Chen [a], Kunpeng Yang [h], Shuntian Wang [c], Ting Liu [f], Yujia Chen [c]

[a] Department of Precision Machinery and Precision Instrumentation, University of Science and Technology of China, Hefei 230026, China
[b] Center for Excellence in Regional Atmospheric Environment, Institute of Urban Environment, Chinese Academy of Sciences, Xiamen 361021, China
[c] Key Lab of Environmental Optics and Technology, Anhui Institute of Optics and Fine Mechanics, Hefei Institutes of Physical Science, Chinese Academy of Sciences, Hefei 230031, China
[d] Key Laboratory of Precision Scientific Instrumentation of Anhui Higher Education Institutes, University of Science and Technology of China, Hefei 230026, China
[e] Anhui Province Key Laboratory of Polar Environment and Global Change, University of Science and Technology of China, Hefei 230026, China
[f] School of Earth and Space Sciences, University of Science and Technology of China, Hefei 230026, China
[g] School of Environmental Science and Optoelectronic Technology, University of Science and Technology of China, Hefei 230026, China
[h] Institute of Physical Science and Information Technology, Anhui University, Hefei 230601, China
[i] School of Environment and Civil Engineering, Jiangnan University, Wuxi 214122, China

ARTICLE INFO

Article history:
Received 13 October 2020
Revised 10 December 2020
Accepted 11 March 2021
Available online 1 July 2021

Keywords:
MAX-DOAS
Stereoscopic monitoring
Regional transport
Ozone production
Control strategy

ABSTRACT

With the coming of the "14th Five-Year Plan," the coordinated control of particulate matter with an aerodynamic diameter no greater than 2.5 μm ($PM_{2.5}$) and O_3 has become a major issue of air pollution prevention and control in China. The stereoscopic monitoring of regional $PM_{2.5}$ and O_3 and their precursors is crucial to achieve coordinated control. However, current monitoring networks are currently inadequate for monitoring the vertical profiles of both $PM_{2.5}$ and O_3 simultaneously and support air quality control. The University of Science and Technology of China (USTC) has established a nationwide ground-based hyperspectral stereoscopic remote sensing network based on multi-axis differential optical absorption spectroscopy (MAX-DOAS) since 2015. This monitoring network provides a significant opportunity for the regional coordinated control of $PM_{2.5}$ and O_3 in China. One-year vertical profiles of aerosol, NO_2 and HCHO monitored from four MAX-DOAS stations installed in four megacities (Beijing, Shanghai, Shenzhen, and Chongqing) were used to characterize their vertical distribution differences in four key regions, Jing–Jin–Ji (JJJ), Yangtze River Delta (YRD), Pearl River Delta (PRD), and Sichuan Basin (SB), respectively. The normalized and yearly averaged aerosol vertical profiles below 400 m in JJJ and PRD exhibit a box shape and a Gaussian shape, respectively, and both show exponential shapes in YRD and SB. The NO_2 vertical profiles in four regions all exhibit exponential shapes because of vehicle emissions. The shape of the HCHO vertical profile in JJJ and PRD was Gaussian, whereas an exponential shape was shown in YRD and SB. Moreover, a regional transport event occurred at an altitude of 600–1000 m was monitored in the southwest–northeast pathway of the North China Plain (NCP) by five MAX-DOAS stations (Shijiazhuang (SJZ), Wangdu (WD), Nancheng (NC), Chinese Academy of Meteorological Sciences (CAMS), and University of Chinese Academy of Sciences (UCAS)) belonging to the above network. The aerosol optical depths (AOD) in these five stations decreased in the order of SJZ > WD > NC > CAMS > UCAS. The short-distance regional transport of NO_2 in the 700–900 m layer was monitored between WD and NC. As an important precursor of secondary aerosol, the peak of NO_2 air mass in WD and NC all occurred 1 h earlier than that of aerosol. This was also observed for the short-distance regional transport of HCHO in the 700–900 m layer between NC and CAMS, which potentially affected the O_3 concentration in Beijing. Finally, CAMS was selected as a typical site to determine the O_3–NO_x–volatile organic compounds (VOCs) sensitivities in vertical space. We found the production of O_3 changed from predominantly VOCs-limited conditions to mainly mixed VOCs–NO_x-limited

* Corresponding author.
E-mail address: xingcz@aiofm.ac.cn (C. Xing).

https://doi.org/10.1016/j.eng.2021.02.019

condition from the 0–100 m layer to the 200–300 m layer. In addition, the downward transport of O_3 could contribute to the increase of ground surface O_3 concentration. This ground-based hyperspectral stereoscopic remote sensing network provide a promising strategy to support management of $PM_{2.5}$ and O_3 and their precursors and conduct attribution of sources.

1. Introduction

Following rapid economic development, air pollution has become a serious threat in China. To tackle the major challenge of improving air quality, the Chinese government has successively disseminated the "Action Plan for Air Pollution Prevention and Control" (the so-called national "Ten Measures of Air") and "Three-Year Action Plan to Win the Blue Sky Defense War" (the "Blue Sky Defense War") since 2013 [1–3]. Following these continuous efforts on emission control and restriction, SO_2 and $PM_{2.5}$ emissions have been considerably decreased by 70% and 46%, respectively, from 2013 to 2019. Although major pollutants such as $PM_{2.5}$ have reduced substantially, O_3 concentrations have maintained an upward trend in recent years [4,5]. The 90th percentile of the daily averaged maximum eight-hour O_3 concentration in 337 main cities of China increased 20.3% from 2013 to 2019. Tropospheric O_3 is produced by emissions of nitrogen oxides (NO_x = NO + NO_2) and volatile organic compounds (VOCs) and their photolysis [6–8]. The emission reduction of NO_x and VOCs was only 26% and 2%, respectively, from 2013 to 2019. In short, China is facing a complex air pollution problem with high $PM_{2.5}$ and O_3 concentrations that developed countries have not experienced. Therefore, it is urgent to carry out stereoscopic monitoring of $PM_{2.5}$, O_3, and their precursors and promote the coordinated control of $PM_{2.5}$ and O_3 compound pollution.

In addition to local emission and secondary formation of air pollutants, regional transport is also a driving force of air pollution that cannot be ignored. Currently, the main technological means being used to study air pollution include *in situ* observation, satellite observation, model simulation, and ground-based remote sensing observations. Since 2012, the Chinese government has successively established a nationwide ground-based air quality monitoring network—China National Environmental Monitoring Center (CNEMC) with 1497 stations to monitor surface concentrations of SO_2, NO_2, CO, PM_{10}, $PM_{2.5}$, and O_3, providing a basis for air quality evaluation and related scientific research [9]. Satellite observations can monitor the horizontal distribution of the vertical column densities (VCDs) of aerosol, NO_2, HCHO, and O_3 at a large scale; however, their temporal and spatial resolution is limited and most of the environmental remote sensing monitoring satellites only overpass the target area once a day, with a maximum spatial resolution of only (3.5×7) km^2 [10–12]. In addition, both CNEMC and satellite technology cannot monitor the vertical futures of atmospheric composition. Moreover, the chemical transport model is an important means to assist atmospheric environmental monitoring, forecasting and research on atmospheric pollution mechanisms; however, inadequate modelling of air pollutants in the vertical has been recognized as an important deficiency. Many important processes that determine formation, conversion, and transport of air pollutants occur above the surface, often in distinct vertical layers between 0 and 2 km above the surface. To compensate for the lack of vertical technology, multiple research units have carried out vertical observations of atmospheric composition using aircraft, unmanned aerial system (UAS), and light detection and ranging (LiDAR) technologies [13–15]. However, LiDAR only can monitor aerosol and O_3 vertical profiles and has a monitoring overlap height. Aircraft and UAS consume considerable labor and material resources and cannot achieve continuous monitoring.

The ground-based hyperspectral stereoscopic remote sensing network is composed of multiple stations. Multi-axis differential optical absorption spectroscopy (MAX-DOAS) provides a promising strategy to learn coordinated control of O_3 and $PM_{2.5}$. It can provide vertical distribution data for $PM_{2.5}$, O_3, and their precursors and help to advance diagnostic understanding and prediction of air pollution. To date, several MAX-DOAS networks have been reported around the world. The University of Bremen, Germany established the Bremian DOAS network for atmospheric measurements (BREDOM) network, including 15 stations distributed throughout Europe and Africa [16]. The Royal Belgian Institute for Space Aeronomy (BIRA-IASB) set up an MAX-DOAS network, including six stations around the world [17]. The Japan Agency for Marine–Earth Science and Technology (JAMSTEC) and European Union established the MAX-DOAS network over Russia and Asia (MADRAS) with seven stations and Network for Observation of Volcanic and Atmospheric Change (NOVAC) with 15 stations [18,19]. A ground-based hyperspectral stereoscopic remote sensing network based on MAX-DOAS with 34 stations coving seven regions of China (north China, east China, south China, southwest China, northwest China, northeast China, and central China) was established by the University of Science and Technology of China (USTC) in 2015. The major purpose of this network is to realize a long-term, continuous, and stereoscopic monitoring of the stereoscopic distribution of atmospheric composition over China. It can make up for the lack of vertical observation capabilities of *in situ* stations and meet the actual needs of precise location of air pollution sources, quantification of regional transmission, and evaluation of the relative contribution of meteorology and emissions to guide air quality management.

In this study, we used one-year observation data of four megacities (Beijing, Shanghai, Shenzhen, and Chongqing) to determine the regional differences of vertical distribution of aerosol, NO_2 and HCHO in Jing–Jin–Ji (JJJ) area, Yangtze River Delta (YRD) area, Pearl River Delta (PRD) area, and Sichuan Basin (SB) area based on above network. A typical transport process with a southwest–northeast pathway over the North China Plain (NCP) was analyzed to reveal the impact of regional transport on air pollution in Beijing. Moreover, O_3–NO_x–VOCs sensitivities in the vertical direction at a one-year time scale in Beijing were determined based on the above network. The development of this ground-based hyperspectral stereoscopic remote sensing network is helpful to promote coordinated control of O_3 and $PM_{2.5}$ over China in the "14th Five-Year Plan" and boost our understanding of air pollution.

2. Methodology and calculation

2.1. Introduction to the network

USTC has organized and complete the construction of a ground-based hyperspectral stereoscopic remote sensing network over China between December 2016 and October 2020. The core instrument within this network is MAX-DOAS. Table 1 shows the geographic distribution and details of the network stations,

Table 1
Geographic of MAX-DOAS network of China. The classification of regions is based on the standards of the Administrative Division of China.

No.	Region	Station (code)	Longitude (°E)	Latitude (°N)	Altitude (m)
1	North China	Chinese Academy of Meteorological Sciences (CAMS)	116.32	39.94	100
2		The Institute of Atmospheric Physics (IAP)	116.37	39.97	100
3		Nancheng (NC)	116.12	39.78	60
4		University of Chinese Academy of Sciences (UCAS)	116.67	40.40	120
5		Gucheng (GC)	115.73	39.14	20
6		Wangdu (WD)	115.15	38.17	35
7		Xianghe (XH)	116.97	39.76	10
8		Shijiazhuang (SJZ)	114.60	37.90	70
9		Shanxi University (SXU)	112.58	37.63	780
10		Inner Mongolia Normal University (IMNU)	111.68	40.80	1040
11	East China	Dongying (DY)	118.98	37.76	2
12		Qingdao (QD)	120.67	36.34	10
13		Taishan (TS)	117.10	36.25	1500
14		Shanghai_Xuhui (SH_XH)	121.43	31.17	3
15		Shanghai_Dianshan Lake (SH_DL)	120.97	31.09	3
16		Nanjing University of Information Science and Technology (NUIST)	118.71	32.20	73
17		Ningbo (NB)	121.89	29.75	10
18		Huaniao Island (HNI)	122.67	30.86	60
19		Huaibei Normal University (HNU)	116.80	33.98	35
20		Anhui University (AHU)	117.18	31.77	30
21		Anhui Meteorological Bureau (AMB)	117.24	31.86	40
22		Hefei Environmental Protection Bureau (HEPB)	117.20	31.78	39
23	South China	Xiamen_Institute of Urban Environment (IUE)	118.05	24.61	340
24		Guangzhou Institute of Geochemistry (GIG)	113.35	23.15	30
25		Southern University of Science and Technology (SUST)	113.99	22.59	40
26	Southwest China	Everest Station (EVS)	86.94	28.36	4276
27		Nam Co Station (NCS)	90.96	30.77	4730
28		Shangri-La Station (SLS)	99.72	28.00	3580
29		Chongqing (CQ)	106.50	29.60	332
30	Northwest China	Lanzhou University (LZU)	103.85	36.04	1600
31		Xi'an (XA)	109.09	34.52	410
32	Northeast China	Juehua Island (JHI)	120.77	40.47	18
33		Liaoning University (LNU)	123.04	41.81	46
34	Central China	Luoyang (LY)	112.45	34.67	100

respectively, which include 34 standard instruments and cover seven major regions of China (ten stations in north China, 12 stations in east China, three stations in south China, four stations in southwest China, two stations in northwest China, two stations in northeast China, and one station in central China). Table 2 presents the observational elements and the instrument detection limit and vertical distribution spatiotemporal resolution of these elements.

2.2. Ground-based hyperspectral stereoscopic remote sensing measurements

2.2.1. Instrument setup

The MAX-DOAS instrument consists of three major parts (Fig. 1): a telescope with an accuracy of < 0.1° and a field of view of < 0.3°, two spectrometers (AvaSpec-ULS2048L-USB2 (Avantes, the Netherlands); ultraviolet (UV) range: 296–408 nm; visible range: 420–565 nm; spectral resolutions: 0.45 nm) with temperature stabilized at 20 °C (deviation < 0.05 °C), and a computer acting as the system controller and data acquisition and transmission unit. The viewing elevation angle and azimuth angle of the telescope are controlled by two stepping motors. The telescope collects scattered sunlight and then the prism reflector and quartz fiber direct it to the spectrometers. Moreover, a charge-coupled device detector camera (ILX511 with 2048 individual pixels (Sony, Japan)) is used to convert the optical signal from analog to digital.

A full elevation sequence consists of 11 angles (i.e., 1°, 2°, 3°, 4°, 5°, 6°, 8°, 10°, 15°, 30°, and 90°), and one sequence takes about 12 min due to the time consuming of the rotation of elevation stepping motor. The settings of exposure time and scan number

Table 2
Observational elements, detection limit, and temporal and spatial resolutions across the network.

Observational element	Detection limit		Resolution	
	SCD	VMR	Temporal	Spatial
O_4	4×10^{41} molec^2·cm^{-5}	—	—	—
Aerosol	—	0.02 km^{-1}	Per vertical profiles: 15 min	Vertical spatial resolution: 100 m
NO_2	7×10^{14} molec·cm^{-2}	30.0 ppt	—	—
HONO	4×10^{14} molec·cm^{-2}	15.0 ppt	—	—
SO_2	7×10^{15} molec·cm^{-2}	300.0 ppt	—	—
HCHO	5×10^{15} molec·cm^{-2}	200.0 ppt	—	—
Glyoxal	3×10^{14} molec·cm^{-2}	20.0 ppt	—	—
BrO	2×10^{13} molec·cm^{-2}	0.7 ppt	—	—
IO	1×10^{13} molec·cm^{-2}	0.6 ppt	—	—
H_2O	1×10^{22} molec·cm^{-2}	0.05%	—	—

SCD: slant column density; VMR: volume mixing ratio; molec: molecule; ppt: part per trillion.

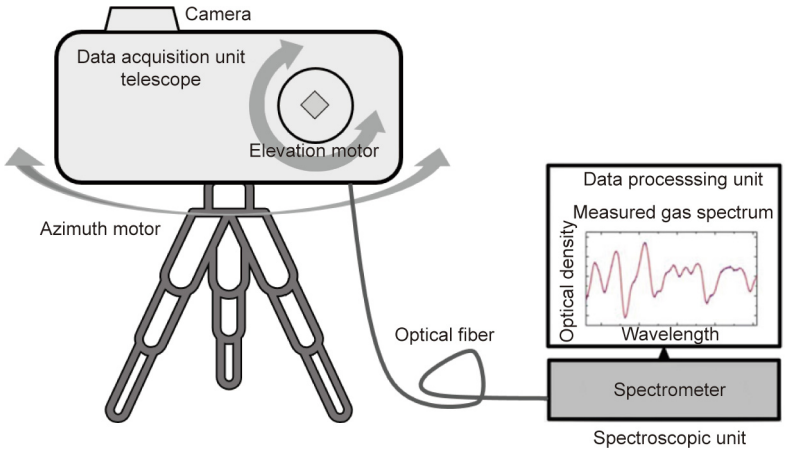

Fig. 1. Schematic view of the MAX-DOAS instrument.

depend on the intensity of the scattered sunlight. The data acquisition unit is controlled by JavaScript to automatically collect scattered sunlight during the daytime and collect dark current and offset during the night. The dark current and offset were removed during the spectral analysis. In order to avoid the strong influence of stratospheric absorbers, the spectra measured with a solar zenith angle (SZA) of > 75° were filtered [20–22].

2.2.2. Spectral analysis

The software QDOAS developed by BIRA-IASB[†] is based on the least squares algorithm, and was used to analyze measured spectra from MAX-DOAS. The zenith spectrum is generally used as a reference spectrum to make differences with off-zenith spectra of each elevation sequence during the retrieval. The direct DOAS fitting results are slant column densities (DSCDs) [23]. Moreover, the ring spectrum was calculated for the measured spectrum with reference to the absorption from the stratosphere. DSCDs of oxygen dimer (O_4) and NO_2 were analyzed in the interval of 338.0–370.0 nm, and the 336.5–359.0 nm wavelength interval was used for HCHO absorption analysis, based on recommended settings from the Cabauw intercomparison campaign for nitrogen dioxide measuring instruments (CINDI) [24,25]. Details of fit settings for O_4, NO_2, and HCHO are listed in Table 3 [26–34]. A typical DOAS fit example of the above three species is shown in Fig. 2. To ensure the validity of the retrieved data, O_4, NO_2, and HCHO DSCDs with a root mean square (RMS) larger than 5×10^{-4} were filtered out. In addition, considering the cloud effect, a threshold obtained through fitting a fifth-order polynomial to color index data at each time was used to filter out DSCDs with a color index less than 10% [35].

2.2.3. Vertical profile retrieval algorithm

The vertical profile inversion algorithm for aerosol and trace gases (i.e., NO_2 and HCHO) was developed based on the optical estimation method (OEM) [36] and employs the radiative transfer model linearized pseudo-spherical vector discrete ordinate radiative transfer models (VLIDORT) as the forward model [37]. The following cost function χ^2 was selected to determine the maximum a posteriori state vector $\boldsymbol{x}$.

$$\chi^2 = (\boldsymbol{y} - \mathrm{F}(\boldsymbol{x},\boldsymbol{b}))^{\mathrm{T}}\boldsymbol{S}_{\varepsilon}^{-1}(\boldsymbol{y} - \mathrm{F}(\boldsymbol{x},\boldsymbol{b})) + (\boldsymbol{x} - \boldsymbol{x}_{\mathrm{a}})^{\mathrm{T}}\boldsymbol{S}_{\mathrm{a}}^{-1}(\boldsymbol{x} - \boldsymbol{x}_{\mathrm{a}}) \quad (1)$$

where $\mathrm{F}(\boldsymbol{x},\boldsymbol{b})$ describes the measurement vector $\boldsymbol{y}$ (measured DSCDs) as a function of the retrieval state vector $\boldsymbol{x}$ (aerosol and trace gases vertical profiles) and true atmospheric state parameters $\boldsymbol{b}$ (i.e., temperature and pressure profiles, albedo, single scattering albedo, asymmetry factor, and Ångström exponent). The temperature and pressure profiles were taken from a climatology database [17]. Aerosol optical properties are selected from the monthly averaged results of the moderate resolution imaging spectroradiometer (MODIS). $\boldsymbol{x}_{\mathrm{a}}$ is the a priori vector. The exponential decreasing shape was selected for the initial a priori profiles of all aerosol and trace gases. In the iteration process, the state profile retrieved from the previous step will be used as the a priori profile for the next step. Moreover, aerosol optical depth (AOD) simulated by weather research and forecasting model coupled with chemistry (WRF–Chem) is also an input priori information in this algorithm. $\boldsymbol{S}_{\mathrm{a}}$ and $\boldsymbol{S}_{\varepsilon}$ describe the covariance matrices of $\boldsymbol{x}_{\mathrm{a}}$ and $\boldsymbol{y}$, respectively. The inversion strategy is based on a Gauss–Newton (GN) scheme. Jacobians of $\mathrm{F}(\boldsymbol{x})$ are used as weighting function in this strategy, which describes the changes of simulated DSCDs of each elevation

Table 3
DOAS settings used for the O_4, NO_2, and HCHO DSCDs' retrieval.

Parameter	Cross sections	Fitting interval			Reference
		O_4	NO_2	HCHO	
Wavelength range[a]	–	338.0–370.0 nm	338.0–370.0 nm	336.5–359.0 nm	–
NO_2	220 K, 294 K, I_0 correction[b] (SCD of 10^{17} molec·cm^{-2})	√	√	√ (only 294 K)	[26]
HCHO	297 K	√	√	√	[27]
O_3	223 K, 243 K, I_0 correction (SCD of 10^{20} molec·cm^{-2})	√	√	√	[28]
O_4	293 K	√	√	√	[29]
BrO	223 K	√	√	√	[30]
H_2O	296 K	√	√	×	[31]
Ring	Ring spectra calculated with QDOAS	√	√	√	[32]
Polynomial degree	–	Order 5	Order 5	Order 5	–
Intensity offset	–	Constant	Constant	Order 1	–

[a] Wavelength calibration: based on a high-resolution solar reference spectrum (SAO2010 solar spectra) [33].
[b] Solar I_0 correction [34].

[†] http://uv–vis.aeronomie.be/software/QDOAS/ (last access: December 15 2020).

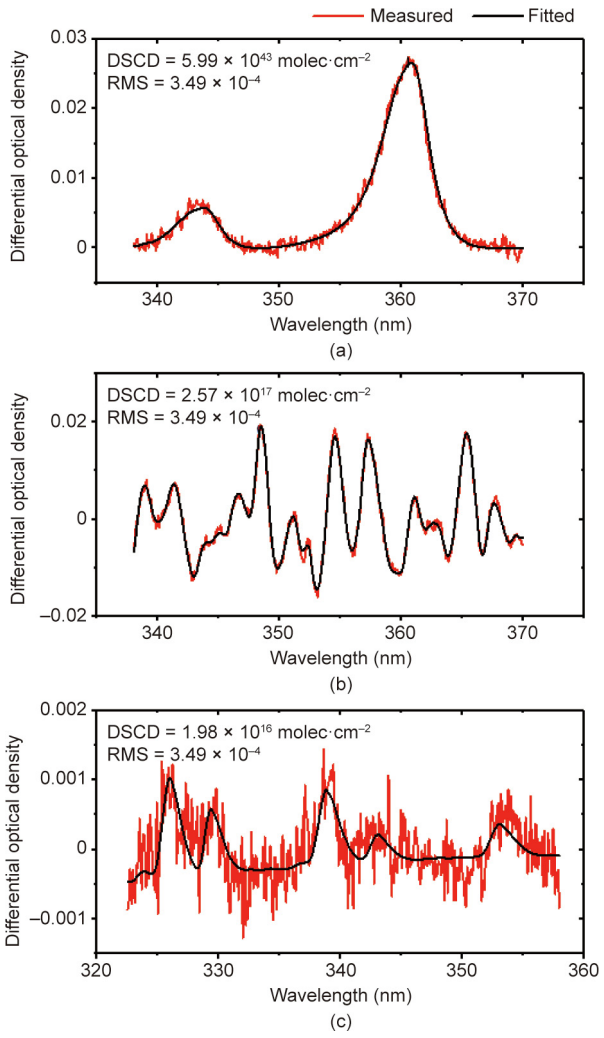

Fig. 2. Typical DOAS spectral fittings for (a) O_4, (b) NO_2, and (c) HCHO. RMS: root mean square.

angle when $\boldsymbol{x}$ within a certain layer is varied. This weighting function calculation process greatly improves the inversion speed compared with the method proposed in the algorithm of Ref. [38]. The determination of air mass factor (AMF) is crucial for the retrieval of trace gases vertical profile. Therefore, two inversion steps were used in this algorithm. The aerosol vertical profile was retrieved first, and then inputted into VLIDORT to participate in retrieval of the vertical profile of the trace gases.

2.3. Ancillary data

Surface $PM_{2.5}$, NO_2, and O_3 concentrations were obtained from the stations of national environmental monitoring network[†]. Surface HCHO concentrations were measured by an AERO LASER AL4021 installed in Peking University (116.31 °E, 39.98 °N). A dynamical-chemical model (WRF–Chem) was used to simulate AOD, wind speed, and direction. A detailed description of this model can be found in Ref. [39]. The horizontal simulation resolution was set to (10 × 10) km^2, and 44 hybrid pressure-sigma levels were set from the ground to 5000 Pa in the vertical direction. The O_3 vertical profiles were monitored by *in situ* instruments installed on the tower located in the IAP with a temporal resolution of 1 h.

[†] https://quotsoft.net/air/ (last access: November 2 2020).

3. Results and discussion

3.1. Regional differences in vertical distribution of aerosol and trace gases

In the last few years, $PM_{2.5}$ and O_3 in China have shown clear characteristics of regional uneven distribution and frequent transmission. Current monitoring networks in China are mainly focused on the ground surface layer [40,41] without monitoring the stereoscopic distribution of $PM_{2.5}$ and O_3 and their precursors, which creates obstacles to the full understanding of their formation to assist air quality management. Therefore, we focused on the vertical structure difference of $PM_{2.5}$ and O_3 and their precursors in four central cities (Beijing, Shanghai, Shenzhen, and Chongqing) to represent the overall conditions in the four major polluted regions of China: the JJJ, YRD, PRD, and SB area.

Four MAX-DOAS stations in the above four central cities, CAMS, SH_XH, SUST, and CQ (Table 1), were selected to study the difference of vertical structure of aerosol, NO_2, and HCHO from 1 March 2019 to 1 March 2020. The CAMS station was selected for retrieved error analysis, and the details are presented in Table 4. Aerosol is the primary pollutant in the atmospheric environment. As shown in Fig. 3(a), a good agreement was observed between the hourly averaged aerosol surface extinction coefficient from the MAX-DOAS retrievals and the *in situ* $PM_{2.5}$ mass concentration in CAMS during the winter of 2019. The correlation coefficient between aerosol and $PM_{2.5}$ depends on the relative humidity (RH) [42], due to the hygroscopic growth of fine particles. To avoid the influence of the RH on the aerosol extinction coefficient in different cities, we normalized the yearly averaged aerosol extinction profiles retrieved from these four stations (Fig. 3(b)). The normalized aerosol extinction vertical profile exhibits a box shape under 400 m in CAMS, indicating that the aerosol particles were well mixed by the turbulence and the weak horizontal transport in the boundary layer height (BLH). Zhang et al. [43] and Liu et al. [44] also found a similar aerosol vertical distribution structure by aircraft measurements in Beijing. The normalized aerosol extinction vertical profile in SH_XH showed an exponential shape. This is likely to be because aerosol pollutants in Shanghai are mainly from local emission, except for the biomass burning season that can be affected by regional transport [45]. The normalized aerosol extinction vertical profile also showed an exponential shape in Chongqing, because the distribution of particulate matter concentrations in SB showed high horizontal homogeneities [46]. The normalized aerosol extinction vertical profile exhibits a Gaussian

Table 4
Estimated errors for retrieved NO_2 and HCHO in different height layers in CAMS station.

Height layers (m)	Component	Random error (%)	Systematic error (%)	Total error (%)
0–200	NO_2	3	7	7.61
	HCHO	4	8	8.94
200–400	NO_2	5	8	9.43
	HCHO	5	10	11.18
400–600	NO_2	6	10	11.66
	HCHO	7	12	13.89
600–800	NO_2	9	12	15.00
	HCHO	11	13	17.03
800–1000	NO_2	11	13	17.03
	HCHO	12	15	19.21
1000–1200	NO_2	11	15	18.60
	HCHO	14	17	22.02
1200–1400	NO_2	12	17	20.81
	HCHO	16	19	24.84
1400–1600	NO_2	14	19	23.60
	HCHO	19	24	30.61

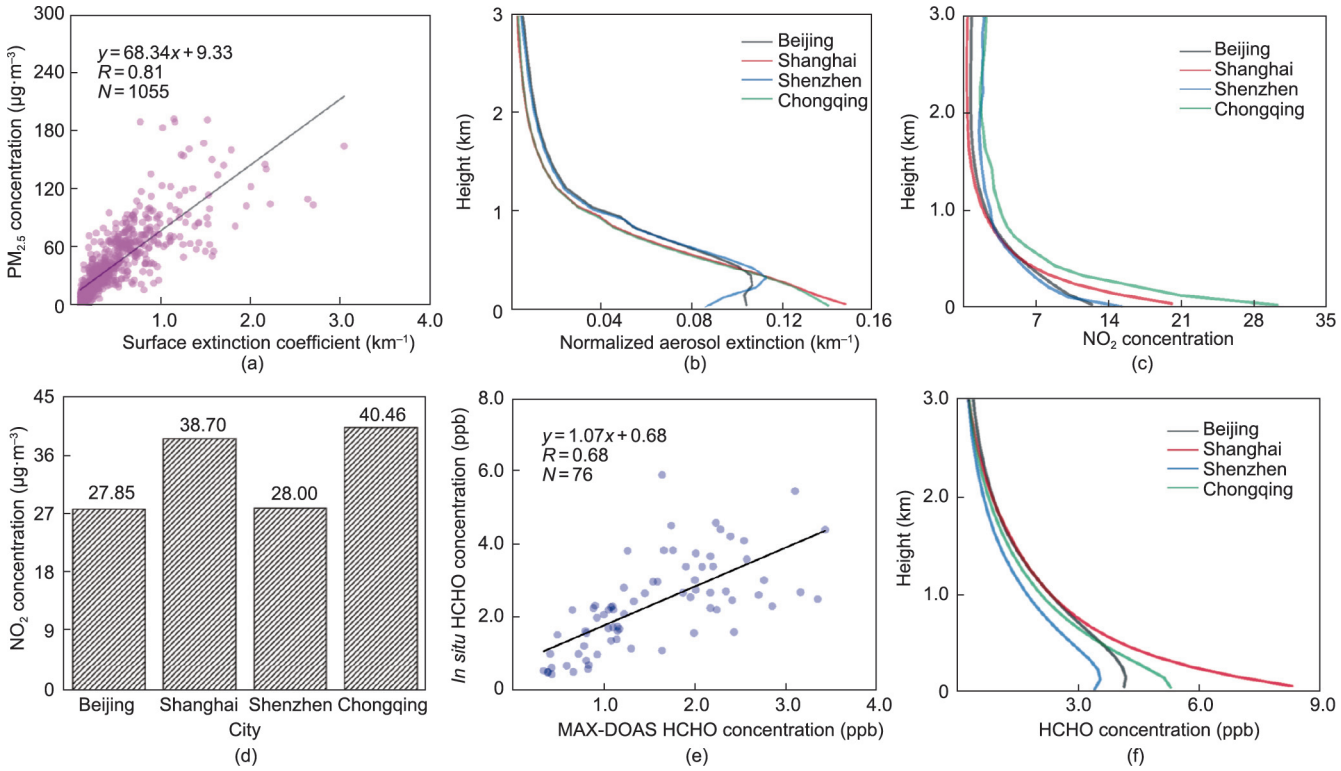

Fig. 3. (a) The scatter plots of surface $PM_{2.5}$ and surface aerosol extinction in Beijing 2019. (b) The normalized and yearly averaged aerosol profiles in Beijing, Shanghai, Shenzhen, and Chongqing. (c) The yearly averaged vertical profiles of NO_2 in the above four cities. (d) The yearly averaged surface NO_2 concentration in above four cities. (e) describes the scatter plots of surface HCHO between *in situ* measured and MAX-DOAS retrieved. *R*: Pearson correlation coefficient. (f) The yearly averaged vertical profiles of HCHO in above four cities. *N*: the number of valid data; ppb: part per billion.

shape in SUST. Liu et al. [47] reported that the regional transport contributes more than 50% to $PM_{2.5}$ concentrations, and local emission only contributed about 10% in Shenzhen. Moreover, the relative contributions from local emissions and regional transport could vary considerably by location. For example, unlike in Shenzhen, Zhao et al. [48] found that the local contribution is around 40%–70% (average 63%) in an industrial city in NCP.

NO_2 and HCHO are the common precursors of secondary aerosol and O_3. Fig. 3(c) shows the yearly averaged NO_2 vertical profiles in the above four stations. The vertical distribution structure of NO_2 in these four stations all exhibit an exponential shape due to the traffic emissions [13,15,49–51]. Moreover, the adverse diffusion condition is also a driving force causing NO_2 to be mainly distributed at the surface in Chongqing [52,53]. Compared with Fig. 3(d), we found that the variation of yearly averaged NO_2 surface concentration from MAX-DOAS retrievals and *in situ* measurements agreed well among the above four stations. The surface NO_2 concentrations at these four stations decreased in the order of CQ > SH_XH > SUST > CAMS. The basin topography hinders the regional diffusion of NO_2, resulting in the highest surface NO_2 concentration among the four stations in CQ. The considerable decrease in the NO_2 concentration in Beijing can be attributed to the powerful emission reduction and regional joint prevention and control measures in recent years and the impact of the coronavirus disease 2019 (COVID-19) in early 2020. As shown in Fig. 3(e), the hourly averaged HCHO surface concentration from the MAX-DOAS retrievals show a good agreement with *in situ* HCHO surface concentration with a Pearson correlation coefficient (*R*) of 0.68 in CAMS from May to October of 2019. Fig. 3(f) shows the yearly averaged HCHO vertical profiles in the above four stations, respectively, which exhibited a Gaussian shape in CAMS, and the highest HCHO concentration was distributed in the 100–200 m layer. That is because the short-distance regional transport of secondary HCHO produced from VOCs photolysis in the southwest of Beijing is also a non-ignorable source of HCHO in CAMS, especially in summer [54,55]. The yearly averaged HCHO shows an exponential shape and the highest surface concentration among above the four stations in SH_XH because the HCHO concentration mainly originates from local primary emission and the photolysis of VOCs [15,56]. The yearly averaged HCHO also showed an exponential shape due to the local industrial emissions in CQ [21]. The yearly averaged HCHO exhibited a Gaussian shape in SUST. Luo et al. [57] reported that the short-distance regional transport of industrial emissions located in northeast Shenzhen is one of the sources of HCHO in SUST.

3.2. Regional transmission analysis of aerosol and the corresponding precursors

The NCP is one of the most polluted regions in China, and several megacities are located in this area (i.e., Beijing, Tianjin, and Shijiazhuang). The NCP is surrounded by Mt. Taihang to the west and Mt. Yan to the north. The semi-basin geographical features and continental monsoon climate mean that regional transport is an important factor affecting air quality in the NCP. The southwest wind belt is the main transport pathway in this region, which can drive $PM_{2.5}$ and O_3 and their precursors to be transmitted in the southwest–northeast direction. Several studies have explored the influences of regional transport over NCP. A community multiscale air quality (CMAQ) model simulation study reported by Streets et al. [58] indicates that unfavorable meteorological conditions can drive the regional transport of $PM_{2.5}$ and O_3 between Beijing and the NCP through this southwest-northeast pathway in summer. Wu et al. [59] used a WRF–Chem simulation to evaluate

the contributions of regional transport from NCP to the elevated $PM_{2.5}$ and O_3 levels in Beijing during summer, and indicated that regional transport contributed 61.5% and 36.6% to $PM_{2.5}$ and O_3, respectively. Based on synchronous *in situ* observations in several cities of the Beijing–Tianjin–Hebei (BTH) region, Ge et al. [60] found the regional transport from southwest to northeast dominated by southwesterly winds is an important role of the daytime elevated $PM_{2.5}$ and O_3 levels. Ge et al. [61] and Zhao et al. [62] also reported a south-to-north transport bell existing over the NCP, which caused regional transport of $PM_{2.5}$ and O_3. However, current *in situ* observations and air quality models are woefully inadequate to fully understand the regional transport of $PM_{2.5}$ and O_3 and their precursors. Air quality models without stereoscopic observation data as support remain large uncertainties in modeling and prediction studies, and the regional transport of air pollutants will be greatly underestimated when using *in situ* observations alone because the transport process is always associated with a high-layer transport belt. A ground-based hyperspectral stereoscopic remote sensing strategy that can monitor the stereoscopic distribution of air pollutants is greatly needed to beat down the disadvantages of the above two techniques in evaluating the regional transport of air pollutants.

Fig. 4 shows the location and topography of the BTH region, and five different MAX-DOAS stations (SJZ, WD, NC, CAMS, and UCAS) of the network are located in the southwest–northeast pathway of this region. A typical southwest–northeast transport process in this region occurring on 5 March 2020, was selected as a case study to indicate the advantages of ground-based hyperspectral stereoscopic remote sensing strategy assisted by the wind field dataset simulated by the WRF model in evaluating transport of air pollutants. Figs. 5(a) and (b) describe the spatial variations of NO_2 and HCHO from the tropospheric monitoring instrument (TROPOMI) in the BTH region on 5 March 2020. NO_2 showed a clear belt distribution along the southwest–northeast pathway, and HCHO showed a continuous regional distribution between NC and CAMS. Figs. 5(c) and (d) present the regional wind field information at 0–20 and 600–1000 m, respectively. The wind direction in these two layers were all from the southwest to northeast along the transmission pathway, and the wind speed in the 600–1000 m layer was about three times that in the 0–20 m layer. Correspondingly, the 600–1000 m layer was the main height of transmission.

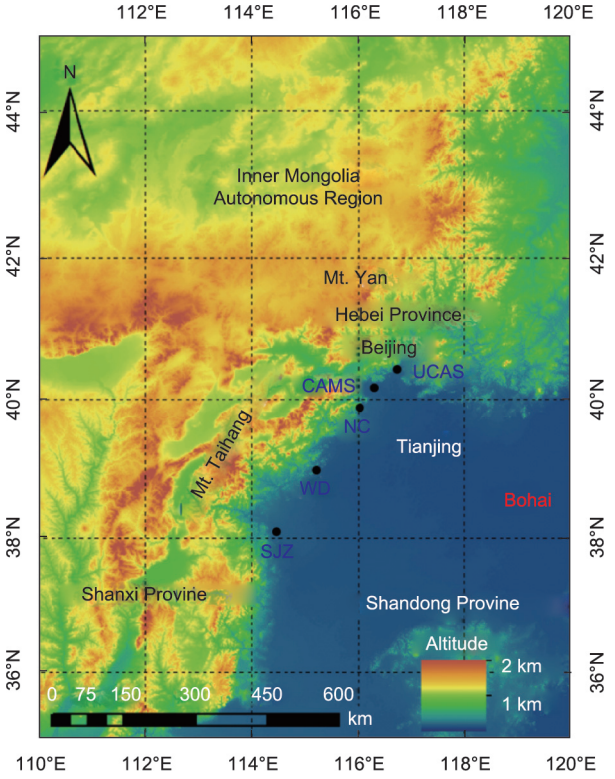

Fig. 4. Study area location, topography, and distribution of MAX-DOAS stations. Black points represent the stations.

Fig. 6 shows the vertical distributions of aerosol, NO_2, and HCHO in the above five stations located along the southwest–northeast pathway on 5 March 2020. It was found that the AOD in these five stations decreased in the order of SJZ > WD > NC > CAMS > UCAS. The high-extinction air mass gradually increased to 700 m after 10:00 in SJZ and was transported to the northeast direction along the transmission pathway driven by the southwest wind. Subsequently, high-extinction aerosols at 800 m were measured in WD after 12:00 and in NC after 13:00. Subsequently, the transmission height of aerosol gradually decreased, and then high-extinction signals were measured near the ground surface after 14:30 in CAMS. Driven by topography and the continuous southwest wind, the high-extinction air mass increased once again and continued to be transported in the northeast direction from CAMS. Finally, the high-extinction aerosol was measured at 500 m in UCAS after 16:00. High-concentration NO_2 near the ground surface was measured in SJZ and CAMS, which was mainly related to the high vehicle emissions in Shijiazhuang and Beijing. There are no clear ground NO_2 emission sources in WD and NC, with high vegetation coverage. Nevertheless, high-concentration NO_2 air masses at 800 m were measured in WD after 11:00 and in NC after 12:00, respectively. At the same transmission height in these two stations, the appearance of high-concentration NO_2 air masses were all about 1 h earlier than those of aerosols. The transport process was accompanied by the formation of secondary inorganic aerosols, based on NO_2 as a main precursor. Moreover, the high-altitude transmission process of HCHO between NC and CAMS stations was also observed (Fig. 6), and mapped to the HCHO transmission belt observed by TROPOMI between NC and CAMS shown in Fig. 5(b). HCHO at NC station is mainly produced by the photolysis of natural source VOCs [63,64]. The air mass carrying secondary-generated HCHO gradually increased to 800 m driven by meteorological elements (i.e., wind and BLH) after 12:00 in NC. Half an hour later, high-concentration HCHO air mass was measured at 800 m in CAMS. The regional transmission of HCHO could affect the variation of O_3 concentration in Beijing to a certain extent.

3.3. O_3–NO_x–VOCs sensitivities in vertical space

In recent years, the continuous increase of O_3 concentration has caused it to become the second major pollutant after $PM_{2.5}$, which has a serious impact on ambient air quality and human health in China. The O_3 in the lower troposphere mainly originates from photochemical reactions of its precursors, regional transport, and the free tropospheric or stratospheric invasion [65]. NO_x and VOCs are two major precursors of O_3. The chemical formation of O_3 depends upon the one (NO_x or VOCs) with substance being inadequate in the reactions. Therefore, the key to controlling O_3 pollution is to effectively control the emissions of its precursors. However, the sensitive types of O_3 formation vary with altitude. We also need to be very clear about the sensitive types of O_3 formation in different heights within the BLH to effectively control O_3 formation. HCHO is an oxidation product of most VOCs and related to their total reactivity [66–68]. It can thus be applied as an indicator of VOCs. Nevertheless, researchers have mainly focused on the sensitive types of O_3 formation at different altitudes. For example, Geng et al. [69] indicated that the formation of surface O_3 is mainly under a VOC-sensitive regime in Shanghai

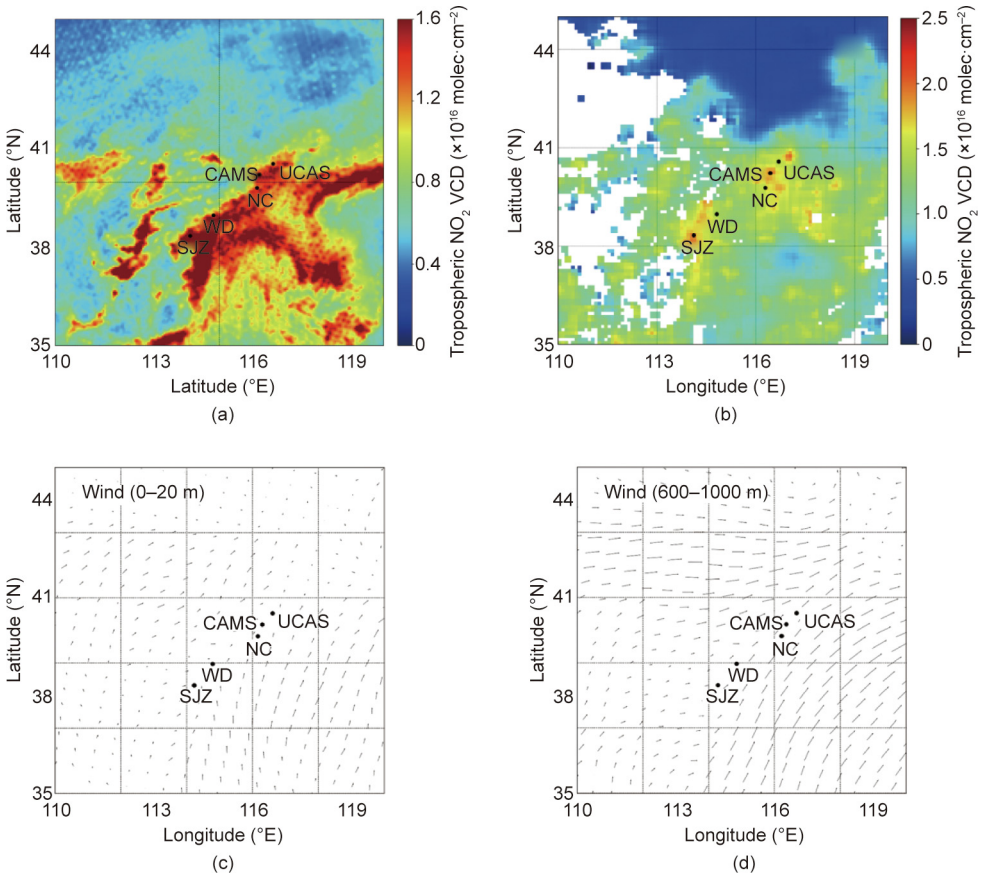

Fig. 5. (a, b) The spatial distribution in NCP of NO_2 and HCHO monitored by TROPOMI on 5 March 2020, respectively. (c, d) The wind field on 0–20 and 600–1000 m layers simulated by WRF on 5 March 2020, respectively. The arrows represent the wind direction.

using *in situ* measured O_3, NO_x, and VOCs. Liu et al. [70] used ozone monitoring instrument (OMI)-observed NO_2 and HCHO tropospheric VCDs to determine the sensitive types of O_3 formation in Beijing during the 2014 Asia–Pacific Economic Cooperation (APEC) summit and 2015 Grand Military Parade.

Observations of NO_2 and HCHO vertical distributions from ground-based hyperspectral stereoscopic remote sensing network can help to investigate the O_3 formation pathways in different regions. In this study, Beijing was selected as a typical city to determine sensitive types of O_3 formation in three different height layers (0–100, 100–200, and 200–300 m) from May to October 2019. The O_3 concentrations in these layers were measured using *in situ* instruments installed in a tower at the IAP. The NO_2 and HCHO concentrations in these three layers were retrieved from MAX-DOAS at the IAP station. With reference to Su et al. [71], the sensitivity thresholds of O_3 formation in these three layers were determined by the slope of the linear regression analysis for O_3 versus the normalized HCHO or NO_2 ratios. Fig. 7 shows the time series of O_3, NO_2, and HCHO all with temporal resolutions of 1 h in these three layers from May to October 2019. As shown in Fig. 8, the sensitive types of O_3 formation were divided into VOCs-limited, VOCs–NO_x-limited, and NO_x-limited. The O_3 production sensitivity regimes in the 0–100, 100–200, and 200–300 m layers are shown in Table 5. In the 0–100 m layer, the chemical sensitivity of local O_3 production is mainly under VOCs-limited conditions, accounting for 71.10% of the effective time of the total observation period. The VOCs–NO_x-limited and NO_x-limited conditions accounted for 16.46% and 12.44%, respectively. The NO_x-limited conditions mainly occurred in July and early October. In the 100–200 m layer, the chemical sensitivity of local O_3 production accounted for 64.31%, 27.02%, and 8.67% under VOCs-limited, VOCs–NO_x-limited, and NO_x-limited conditions, respectively. In the 200–300 m layer, the chemical sensitivity of local O_3 production accounted for 56.10%, 35.55%, and 8.35% under VOCs-limited, VOCs–NO_x-limited, and NO_x-limited conditions, respectively. The proportions of VOCs-limited, and NO_x-limited conditions of the chemical sensitivity of local O_3 production gradually decreased from the 0–100 m layer to the 200–300 m layer, whereas the proportion of VOCs–NO_x-limited conditions showed the opposite trend.

The O_3, NO_2, and HCHO vertical profiles measured at 14:00 on 2 July 2019 were selected as a typical case to study the O_3–NO_x–VOCs sensitivities in different layers. As shown in Fig. 9(a), a high O_3 concentration was observed in the 0–100 m layer, and the corresponding chemical sensitivity of local O_3 production in this layer indicated an NO_x-limited regime. We also found that the NO_2 concentration at this layer also had a high value (Fig. 9(b)). Fig. 10(a) depicts the O_3 vertical profile at 14:00 on 2 July 2019 and the averaged O_3 vertical profile of July 2019. The averaged concentration of the former was approximately twice that of the latter, especially in the 0–100 m layer, in which the former was approximately 1.99 times higher than that of the later. In order to estimate the influence of the high O_3 concentration in the 0–100 m layer to the ground surface, the diurnal cycle of ground surface concentration of O_3 on 2 July 2019 was compared with that the monthly average diurnal cycle for July 2019 (Fig. 10(b)). The monthly averaged diurnal cycle of O_3 peaked at 14:00 and

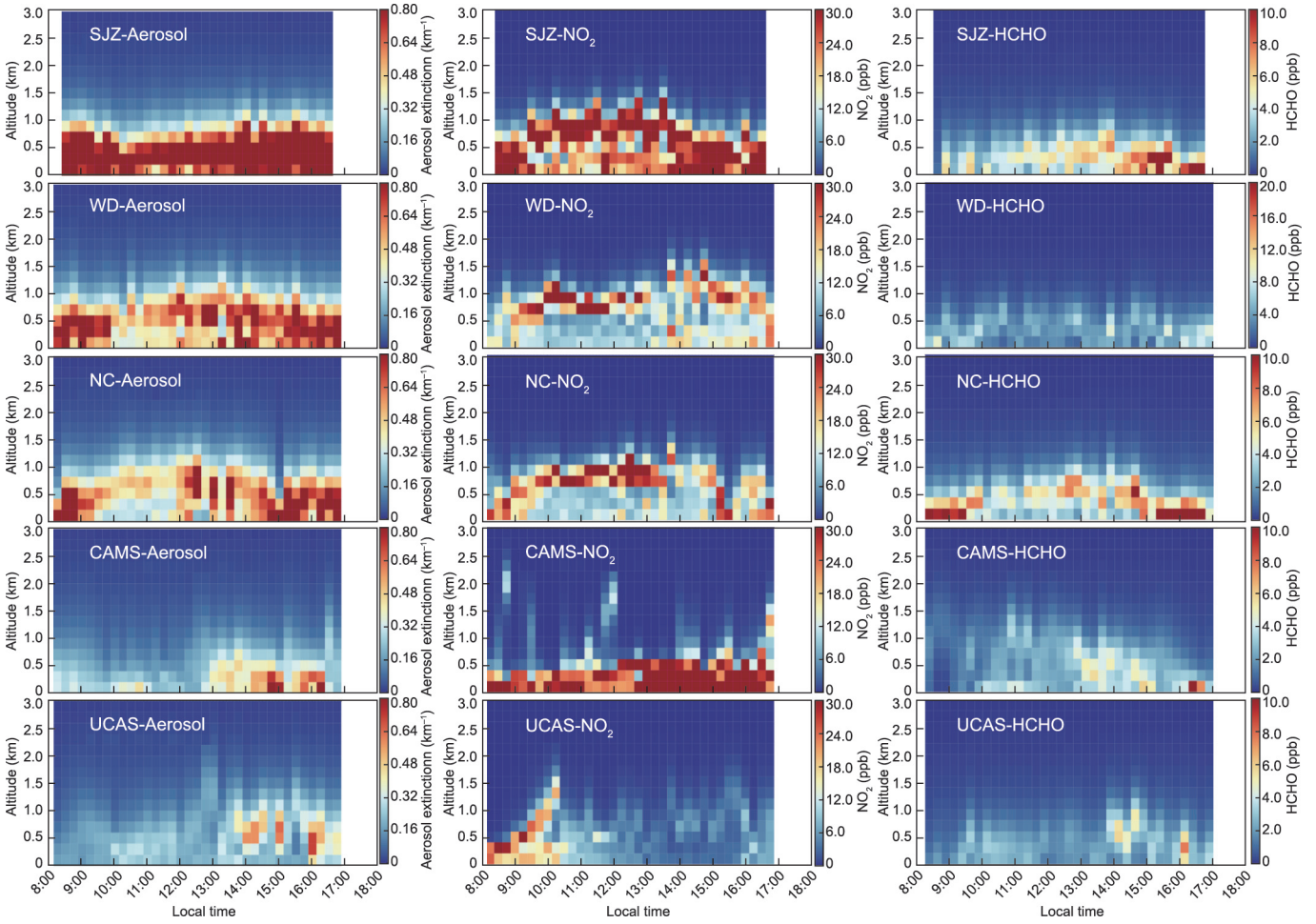

Fig. 6. Vertical profiles of aerosol, NO_2, and HCHO in SJZ, WD, NC, CAMS, and UCAS stations on 5 March 2020, respectively.

decreased thereafter; however, the diurnal cycle of O_3 on 2 July 2019 also peaked at 14:00, but continued to increase at least until 15:00. This indicates that the downward transport of O_3 in BLH could contribute to the increase of the ground surface O_3 concentration.

4. Conclusions

A ground-based hyperspectral stereoscopic remote sensing network based on MAX-DOAS was established by USTC, and vertical profiles of aerosol, O_3, and their common precursors were monitored. Firstly, we explored the differences in the vertical structure of aerosols, NO_2, and HCHO in four typical pollution regions (JJJ, YRD, PRD, and SB). The structure of aerosol vertical profile showed a box shape under 400 m in JJJ, due to the regional transport and the effect of BLH. Given that the regional transport contributed more than 50% to $PM_{2.5}$ in the SUST station, the vertical profile exhibits a Gaussian shape in PRD. The vertical profiles in PRD and SB exhibit exponential shape, due to the contribution of local emissions and the limitation of regional diffusion conditions. The structure of NO_2 vertical profiles in the above four regions were all exponential because of vehicle emissions. The yearly averaged vertical profile of HCHO shows a Gaussian shape attributing to the short-distance transport from the southwest direction in CAMS and the regional transport from northeast industrial emissions in SUST. The vertical structure of HCHO exhibited an exponential shape because of the local emissions and local photolysis of VOCs in SH_XH and the local industrial emission in CQ.

Second, the southwest–northeast pathway of NCP was identified as a typical regional transport pathway of atmospheric composition. Five MAX-DOAS stations (SJZ, WD, NC, CAMS, and UCAS) were installed in this pathway. A typical southwest–northeast transport process in the NCP region occurred on 5 March 2020. Combining the TROPOMI NO_2 VCDs and the daily averaged WRF wind field information for this day, we found that the 600–1000 m layer was the main height of transmission. The AOD in these five stations decreased in the order of SJZ > WD > NC > CAMS > UCAS. The extinction air mass gradually upward 700 m from the surface in SJZ. Subsequently, the aerosol extinction belts were monitored in the 600–1000 m layer in both WD and NC, and there was a 1 h offset the time of its appearance between these two stations. The extinction air mass was pushed down to the surface in CAMS, and then upward to 500 m again and transported to the UCAS station. Moreover, the short-distance regional transport processes of NO_2 and HCHO in 700–900 m layer were monitored between WD and NC and between NC and CAMS. The maximum NO_2 air mass in WD and NC all occurred 1 h earlier than that of aerosol, and contributed to secondary aerosol formation during the transmission. The short-

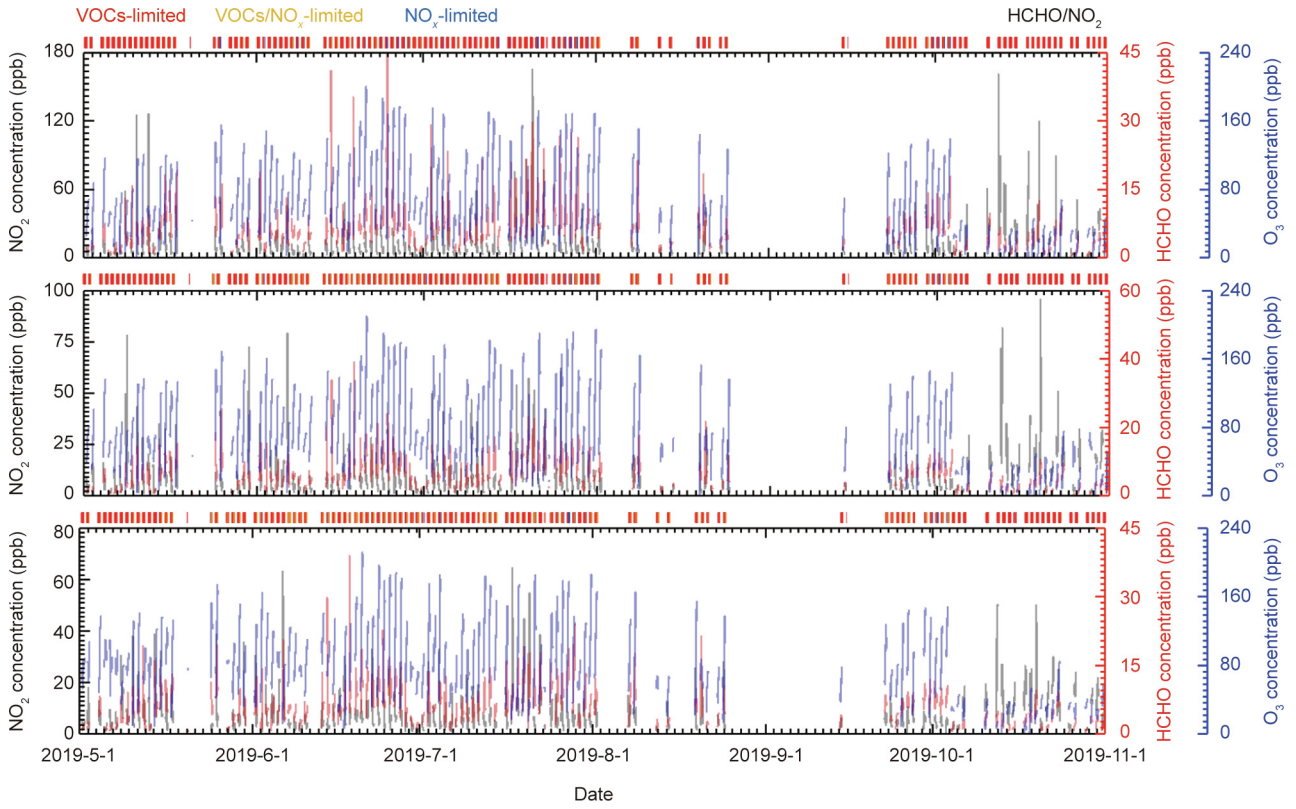

Fig. 7. The time series of NO_2, HCHO, O_3, and the O_3 production sensitivity on (a) 0–100, (b) 100–200, and (c) 200–300 m layers, respectively.

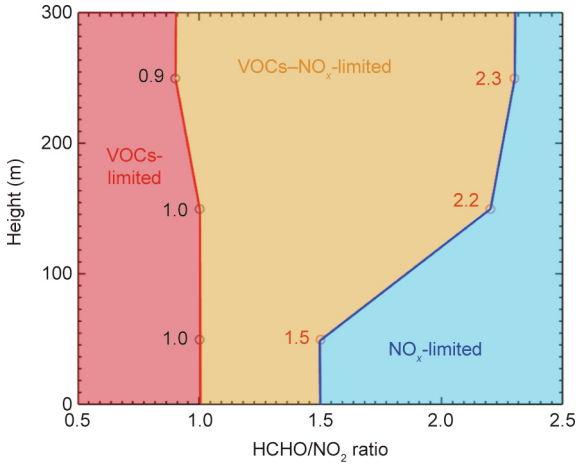

Fig. 8. O_3 production sensitivity regimes in 0–100, 100–200, and 200–300 m layers.

distance regional transport of HCHO potentially affected the O_3 concentration in Beijing.

Third, we selected CAMS as a typical site to learn O_3–NO_x–VOCs sensitivities in three different layers (0–100, 100–200, and 200–300 m) from May to October, 2019. The proportions of VOCs-limited and NO_x-limited conditions of the chemical sensitivity of local O_3 production gradually decreased from 0–100 m layer to 200–300 m layer, whereas the proportion of VOCs–NO_x-limited condition showed the opposite trend. A case study describing a high concentration of O_3 in the 100–200 m layer on July 2, 2019 revealed that the downward transport of O_3 could contribute to the increase of ground surface O_3 concentration. This suggest that the government needs to control the increase of O_3 concentration in different altitude layers and different regions.

Table 5
O_3 production sensitivity regimes in 0–100, 100–200, and 200–300 m height layers.

Height layer (m)	VOCs-limited	VOCs–NO_x-limited	NO_x-limited
0–100	HCHO/$NO_2 \leq 1.0$	$1.0 <$ HCHO/$NO_2 < 1.5$	HCHO/$NO_2 \geq 1.5$
100–200	HCHO/$NO_2 \leq 1.0$	$1.0 <$ HCHO/$NO_2 < 2.2$	HCHO/$NO_2 \geq 2.2$
200–300	HCHO/$NO_2 \leq 0.9$	$0.9 <$ HCHO/$NO_2 < 2.3$	HCHO/$NO_2 \geq 2.3$

Acknowledgments

This research is supported by grants from the National Key Research and Development Program of China (2018YFC0213104), Project supported by the Presidential Foundation of the Hefei Institutes of Physical Science, Chinese Academy Sciences, China—"Spark" (YZJJ2021QN06), National Natural Science Foundation of China (41722501, 91544212, 51778596, 41575021, 41977184, and 41875043), National Key Research and Development Program of China (2017YFC0210002, 2016YFC0203302, and 2017YFC0212800), Anhui Science and Technology Major Project (18030801111), the Strategic Priority Research Program of the Chinese Academy of Sciences (XDA23020301), the National Key

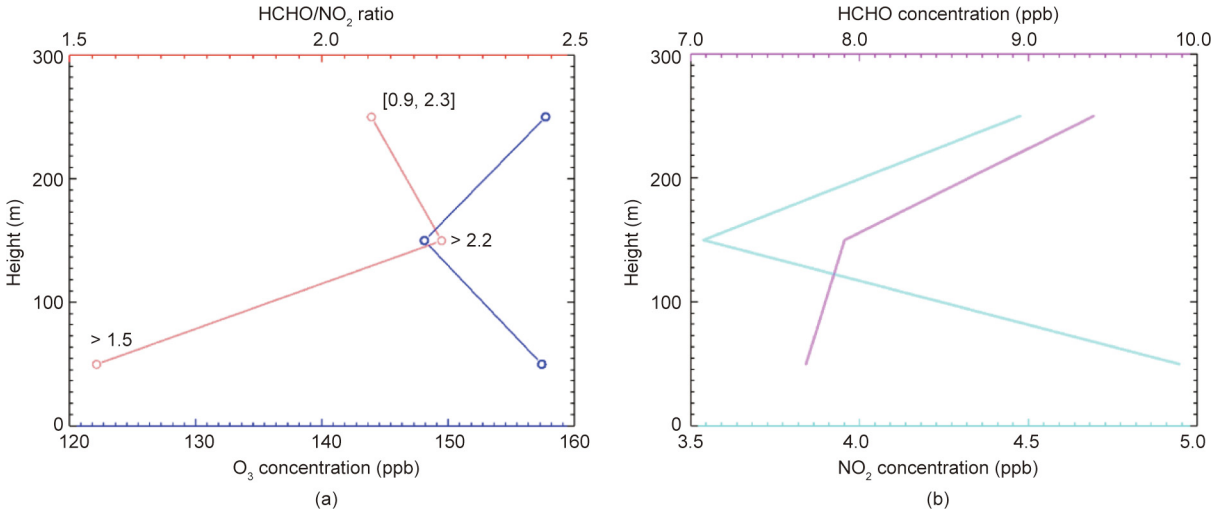

Fig. 9. (a) The vertical distribution of O_3 and HCHO/NO_2 ratios; and (b) the vertical distribution of NO_2 and HCHO at 14:00 on 2 July 2019.

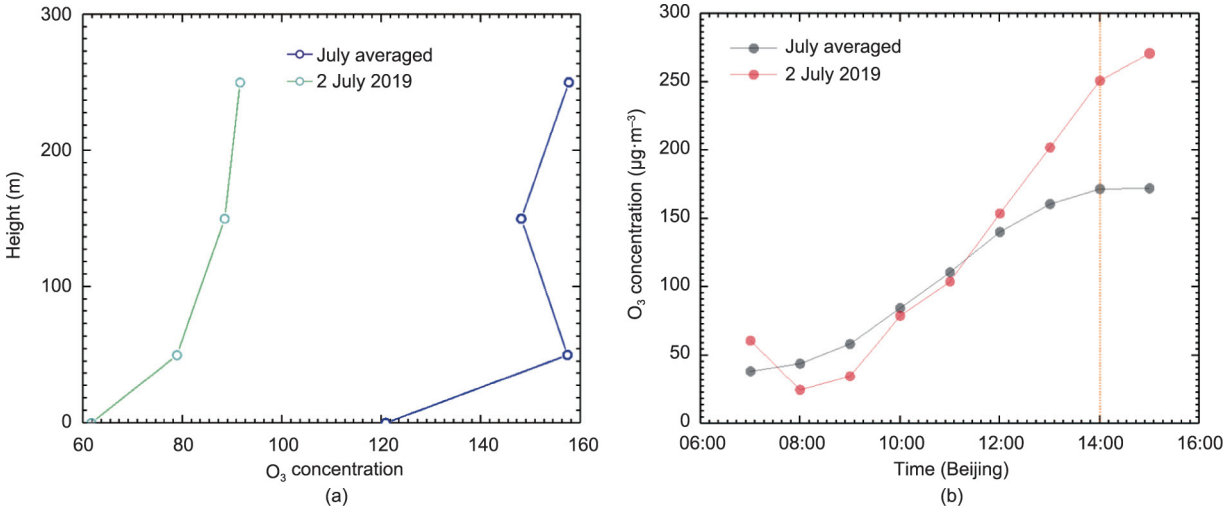

Fig. 10. (a) The monthly averaged O_3 profile on July 2019 and the O_3 profile at 14:00 on July 2, 2019. (b) The time series of monthly averaged surface O_3 on July 2019 and the time series of surface O_3 on 2 July 2019.

Project for Causes and Control of Heavy Air Pollution (DQGG0102 and DQGG0205), the National High-Resolution Earth Observation Project of China (05-Y30B01-9001-19/20-3), and Civil Aerospace Technology Advance Research Project (Y7K00100KJ). From 0–100 and 200–300 m layers, the production of O_3 changed from predominantly VOCs-limited condition to mainly mixed VOCs–NO_x-limited condition.

Compliance with ethics guidelines

Cheng Liu, Chengzhi Xing, Qihou Hu, Qihua Li, Haoran Liu, Qianqian Hong, Wei Tan, Xiangguang Ji, Hua Lin, Chuan Lu, Jinan Lin, Hanyang Liu, Shaocong Wei, Jian Chen, Kunpeng Yang, Shuntian Wang, Ting Liu, and Yujia Chen declare that they have no conflict of interest or financial conflicts to disclose.

References

[1] Feng Y, Ning M, Lei Yu, Sun Y, Liu W, Wang J. Defending blue sky in China: effectiveness of the "Air Pollution Prevention and Control Action Plan" on air quality improvements from 2013 to 2017. J Environ Manage 2019;252:109603.
[2] Maji KJ, Li VOK, Lam JCK. Effects of China's current Air Pollution Prevention and Control Action Plan on air pollution patterns, health risks and mortalities in Beijing 2014–2018. Chemosphere 2020;260:127572.
[3] Jiang X, Li G, Fu W. Government environmental governance, structural adjustment and air quality: a quasi-natural experiment based on the Three-Year Action Plan to Win the Blue Sky Defense War. J Environ Manage 2021;277:111470.
[4] Fan H, Zhao C, Yang Y. A comprehensive analysis of the spatio–temporal variation of urban air pollution in China during 2014–2018. Atmos Envion 2020;220:117066.
[5] Zhang K, Zhao C, Fan H, Yang Y, Sun Y. Toward understanding the differences of $PM_{2.5}$ characteristics among five China urban cities. Asia–Pac J Atmos Sci 2020;56:493–502.
[6] Gao C, Xiu A, Zhang X, Chen W, Liu Y, Zhao H, et al. Spatiotemporal characteristics of ozone pollution and policy implications in northeast China. Atmos Pollut Res 2020;11(2):357–69.
[7] Jin X, Fiore A, Boersma KF, Smedt ID, Valin L. Inferring changes in summertime surface ozone–NO_x–VOC Chemistry over US urban areas from two decades of satellite and ground-based observations. Environ Sci Technol 2020;54(11):6518–29.
[8] Tadic I, Crowley JN, Dienhart D, Eger P, Harder H, Hottmann B, et al. Net ozone production and its relationship to nitrogen oxides and volatile organic compounds in the marine boundary layer around the Arabian Peninsula. Atmos Chem Phys 2020;20(11):6769–87.
[9] Kong L, Tang X, Zhu J, Wang Z, Li J, Wu H, et al. A six-year long (2013–2018) high-resolution air quality reanalysis dataset over China base on the assimilation of surface observations from CNEMC. Earth Syst Sci Data 2021;13:529–70.

[10] Zheng C, Zhao C, Li Y, Wu X, Zhang K, Gao J, et al. Spatial and temporal distribution of NO_2 and SO_2 in Inner Mongolia urban agglomeration obtained from satellite remote sensing and ground observations. Atmos Environ 2018;188:50–9.
[11] Su W, Liu C, Chan KL, Hu Q, Liu H, Ji X, et al. A improved TROPOMI tropospheric HCHO retrieval over China. Atmos Meas Tech 2020;13(11):6271–92.
[12] Liu X, Bhartia PK, Chance K, Froidevaux L, Spurr RJD, Kurosu TP. Validation of Ozone Monitoring Instrument (OMI) ozone profiles and stratospheric ozone columns with Microwave Limb Sounder (MLS) measurements. Atmos Chem Phys 2010;10(5):2539–49.
[13] Zhang K, Zhou L, Fu Q, Yan L, Bian Q, Wang D, et al. Vertical distribution of ozone over Shanghai during late spring: a balloon borne observation. Atmos Environ 2019;208:48–60.
[14] Li XB, Peng ZR, Lu QC, Wang D, Hu XM, Wang D, et al. Evaluation of unmanned aerial system in measuring lower tropospheric ozone and fine aerosol particles using portable monitors. Atmos Environ 2020;222:117134.
[15] Xing C, Liu C, Wang S, Chan KL, Gao Y, Huang X, et al. Observations of the vertical distributions of summertime atmospheric pollutants and the corresponding ozone production in Shanghai, China. Atmos Chem Phys 2017;17(23):14275–89.
[16] Richter A, Adukpo D, Fietkau S, Heckel A, Ladstätter-Weißenmayer A, Löwe A, et al. SCIAMACHY validation using ground-based DOAS measurements of the university of Bremen BREDOM network. In: Proceedings of the ENVISAT Validation Workshop; 2002 Dec 9–13; Frascati, Italy. Frascati: ESRIN; 2002.
[17] Clémer K, Van Roozendael M, Fayt C, Hendrick F, Hermans C, Pinardi G, et al. Multiple wavelength retrieval of tropospheric aerosol optical properties from MAX-DOAS measurements in Beijing. Atmos Meas Tech 2010;3(4):863–78.
[18] Kanaya Y, Irie H, Takashima H, Iwabuchi H, Akimoto H, Sudo K, et al. Long-term MAX-DOAS network observations of NO_2 in Russia and Asia (MADRAS) during the period 2007–2012: instrumentation, elucidation of climatology, and comparisons with OMI satellite observations and global model simulations. Atmos Chem Phys 2014;14:7909–27.
[19] Galle B, Johansson M, Rivera C, Zhang Y, Kihlman M, Kern C, et al. Network for observation of volcanic and atmospheric change (NOVAC)—a global network for volcanic gas monitoring: network layout and instrument description. J Geophys Res 2010;115(D5):D05304.
[20] Xing C, Liu C, Wang S, Hu Q, Liu H, Tan W, et al. A new method to determine the aerosol optical properties from multiple-wavelength O_4 absorptions by MAX-DOAS observation. Atmos Meas Tech 2019;12(6):3289–302.
[21] Xing C, Liu C, Hu Q, Fu Q, Lin H, Wang S, et al. Identifying the wintertime sources of volatile organic compounds (VOCs) from MAX-DOAS measured formaldehyde and glyoxal in Chongqing, southwest China. Sci Total Environ 2020;715:136258.
[22] Wang T, Hendrick F, Wang P, Tang G, Clémer K, Yu H, et al. Evaluation of tropospheric SO_2 retrieved from MAX-DOAS measurements in Xianghe, China. Atmos Chem Phys 2014;14(20):11149–64.
[23] Wagner T, Beirle S, Brauers T, Deutschmann T, Frieß U, Hak C, et al. Inversion of tropospheric profiles of aerosol extinction and HCHO and NO_2 mixing ratios from MAX-DOAS observations in Milano during the summer of 2003 and comparison with independent data sets. Atmos Meas Tech 2011;4(12):2685–715.
[24] Roscoe HK, Van Roozendael M, Fayt C, du Piesanie A, Abuhassan N, Adams C, et al. Intercomparison of slant column measurements of NO_2 and O_4 by MAX-DOAS and zenith-sky UV and visible spectrometers. Atmos Meas Tech 2010;3(6):1629–46.
[25] Karin K, Van Roozendael M, Francois H, Arnoud A, Ermioni D, Frieß U, et al. Intercomparison of NO_2, O_4, O_3 and HCHO slant column measurements by MAX-DOAS and zenith-sky UV–visible spectrometers during the CINDI-2 campaign. Atmos Meas Tech Disc 2019;157:1–58.
[26] Vandaele AC, Hermans C, Simon PC, Carleer M, Colin R, Fally S, et al. Measurements of the NO_2 absorption cross-section from 42 000 cm^{-1} to 10 000 cm^{-1} (238–1000 nm) at 220 K and 294 K. J Quant Spectrosc Ra 1998;59(3–5):171–84.
[27] Meller R, Moortgat GK. Temperature dependence of the absorption cross sections of formaldehyde between 223 and 323 K in the wavelength range 225–375 nm. J Geophys Res 2000;105(D6):7089–101.
[28] Serdyuchenko A, Gorshelev V, Weber M, Chehade W, Burrows JP. High spectral resolution ozone absorption cross-sections—part 2: temperature dependence. Atmos Meas Tech 2014;7(2):625–36.
[29] Thalman R, Volkamer R. Temperature dependent absorption cross-sections of O_2–O_2 collision pairs between 340 and 630 nm and at atmospherically relevant pressure. Phys Chem Chem Phys 2013;15(37):15371–81.
[30] Fleischmann OC, Hartmann M, Burrows JP, Orphal J. New ultraviolet absorption cross-sections of BrO at atmospheric temperatures measured by time-windowing Fourier transform spectroscopy. J Photoch Photobio A 2004;168(1–2):117–32.
[31] Rothman LS, Gordon IE, Barber RJ, Dothe H, Gamache RR, Goldman A, et al. HITEMP, the high-temperature molecular spectroscopic database. J Quant Spectrosc Ra 2010;111(15):2139–50.
[32] Chance KV, Spurr RJD. Ring effect studies: rayleigh scattering, including molecular parameters for rotational Raman scattering, and the Fraunhofer spectrum. Appl Opt 1997;36(21):5224–30.
[33] Chance K, Kurucz RL. An improved high-resolution solar reference spectrum for earth's atmosphere measurements in the ultraviolet, visible, and near infrared. J Quant Spectrosc Ra 2010;111(9):1289–95.
[34] Aliwell S, Van Roozendael M, Johnston P, Richter A, Wagner T, Arlander D, et al. Analysis for BrO in zenith-sky spectra: an intercomparison exercise for analysis improvement. J Geophys Res 2002;107(D14):4199.
[35] Wagner T, Beirle S, Remmers J, Shaiganfar R, Wang Y. Absolute calibration of the colour index and O_4 absorption derived from Multi Axis (MAX-) DOAS measurements and their application to a standardised cloud classification algorithm. Atmos Meas Tech 2016;9(9):4803–23.
[36] Rodgers CD. Inverse methods for atmospheric sounding: theory and practice. Singapore–New Jersey–London–Hong Kong: World Scientific Publishing; 2000.
[37] Spurr RJD. VLIDORT: a linearized pseudo-spherical vector discrete ordinate radiative transfer code for forward model and retrieval studies in multilayer multiple scattering media. J Quant Spectrosc RA 2006;102(2):316–42.
[38] Frieß U, Monks PS, Remedios JJ, Rozanov A, Sinreich R, Wagner T, et al. MAX-DOAS O_4 measurements: a new technique to derive information on atmospheric aerosols: 2. modeling studies. J Geophys Res 2006;111(D14):D14203.
[39] Grell GA, Peckham SE, Schmitz R, McKeen SA, Frost G, Skamarock WC, et al. Fully coupled "online" chemistry within the WRF model. Atmos Environ 2005;39(37):6957–75.
[40] Xin J, Wang Y, Pan Y, Ji D, Liu Z, Wen T, et al. The campaign on atmospheric aerosol research network of China: CARE-China. Bull Am Meteorol Soc 2015;96(7):1137–55.
[41] Dao X, Lin Y, Cao F, Di S, Hong Y, Xing G, et al. Introduction to the national aerosol chemical composition monitoring network of China: objectives, current status, and outlook. Bull Am Meteorol Soc 2019;100(12):ES337–51.
[42] Lv L, Liu W, Zhang T, Chen Z, Dong Y, Fan G, et al. Observations of particle extinction, $PM_{2.5}$ mass concentration profile and flux in north China based on mobile lidar technique. Atmos Environ 2017;164:360–9.
[43] Zhang Q, Ma X, Tie X, Huang M, Zhao C. Vertical distributions of aerosols under different weather conditions: analysis of *in-situ* aircraft measurements in Beijing, China. Atmos Environ 2009;43(34):5526–35.
[44] Liu P, Zhao C, Liu P, Deng Z, Huang M, Ma X, et al. Aircraft study of aerosol vertical distributions over Beijing and their optical properties. Tellus B Chem Phys Meteorol 2009;61(5):756–67.
[45] Liu Q, He Q, Fang S, Guang Y, Ma C, Chen Y, et al. Vertical distribution of ambient aerosol extinctive properties during haze and haze-free periods based on the micro-pulse lidar observation in Shanghai. Sci Total Environ 2017;574:1502–11.
[46] Ning G, Wang S, Ma M, Ni C, Shang Z, Wang J, et al. Characteristics of air pollution in different zones of Sichuan Basin, China. Sci Total Environ 2018;612:975–84.
[47] Liu C, He L, Pi D, Zhao J, Lin L, He P, et al. Integrating LIDAR data and four-dimensional flux method to analyzing the transmission of $PM_{2.5}$ in Shenzhen. Phys Chem Earth 2019;110:81–8.
[48] Zhao C, Wang Y, Shi X, Zhang D, Wang C, Jiang JH, et al. Estimating the contribution of local primary emissions to particulate pollution using high-density station observations. JGR Atmos 2019;124(3):1648–61.
[49] Vlemmix T, Hendrick F, Pinardi G, De Smedt I, Fayt C, Hermans C, et al. MAX-DOAS observations of aerosols, formaldehyde and nitrogen dioxide in the Beijing area: comparison of two profile retrieval approaches. Atmos Meas Tech 2015;8(2):941–63.
[50] Chan KL, Wiegner M, Wenig M, Pöhler D. Observations of tropospheric aerosols and NO_2 in Hong Kong over 5 years using ground based MAX-DOAS. Sci Total Environ 2018;619-620:1545–56.
[51] Li L, Lu C, Chan P, Zhang X, Yang H, Lan Z, et al. Tower observed vertical distribution of $PM_{2.5}$, O_3 and NO_x in the Pearl River Delta. Atmos Environ 2020;220:117083.
[52] Wang QW, Tan ZM. Multi-scale topographic control of southwest vortex formation in Tibetan Plateau region in an idealized simulation. J Geophys Res Atmos 2014;119(20):11543–61.
[53] Yu S, Gao W, Xiao D, Peng J. Observational facts regarding the joint activities of the southwest vortex and plateau vortex after its departure from the Tibetan Plateau. Adv Atmos Sci 2016;33(1):34–46.
[54] Lee H, Ryu J, Irie H, Jang SH, Park J, Choi W, et al. Investigations of the diurnal variation of vertical HCHO profiles based on MAX-DOAS measurements in Beijing: comparisons with OMI vertical column data. Atmosphere 2015;6(11):1816–32.
[55] Wang Y, Dörner S, Donner S, Böhnke S, De Smedt I, Dickerson RR, et al. Vertical profiles of NO_2, SO_2, HONO, HCHO, CHOCHO and aerosols derived from MAX-DOAS measurements at a rural site in the central western North China Plain and their relation to emission sources and effects of regional transport. Atmos Chem Phys 2019;19(8):5417–49.
[56] Wang Y, Lampel J, Xie P, Beirle S, Li A, Wu D, et al. Ground-based MAX-DOAS observations of tropospheric aerosols, NO_2, SO_2 and HCHO in Wuxi, China, from 2011 to 2014. Atmos Chem Phys 2017;17(3):2189–215.
[57] Luo Y, Dou Ke, Fan G, Huang S, Si F, Zhou H, et al. Vertical distributions of tropospheric formaldehyde, nitrogen dioxide, ozone and aerosol in southern China by ground-based MAX-DOAS and LIDAR measurements during PRIDE-GBA 2018 campaign. Atmos Environ 2020;226:117384.
[58] Streets DG, Fu JS, Jang CJ, Hao J, He K, Tang X, et al. Air quality during the 2008 Beijing Olympic Games. Atmos Environ 2007;41(3):480–92.
[59] Wu J, Li G, Cao J, Bei N, Wang Y, Feng T, et al. Contributions of trans-boundary transport to summertime air quality in Beijing. China. Atmos Chem Phys 2017;17(3):2035–51.

[60] Ge B, Wang Z, Lin W, Xu X, Li J, Ji D, et al. Air pollution over the North China Plain and its implication of regional transport: a new sight from the observed evidences. Environ Pollut 2018;234:29–38.
[61] Ge BZ, Xu XB, Lin WL, Li J, Wang ZF. Impact of the regional transport of urban Beijing pollutants on downwind areas in summer: ozone production efficiency analysis. Tellus B Chem Phys Meteorol 2012;64(1):17348.
[62] Zhao C, Wang Y, Zeng T. East China plains: a "basin" of ozone pollution. Environ Sci Technol 2009;43(6):1911–5.
[63] Zhu S, Li X, Yu C, Wang H, Wang Y, Miao J. Spatiotemporal variations in satellite-based formaldehyde (HCHO) in the Beijing–Tianjin–Hebei region in China from 2005 to 2015. Atmosphere 2018;9(1):5.
[64] Liu Y, Song M, Liu X, Zhang Y, Hui L, Kong L, et al. Characterization and sources of volatile organic compounds (VOCs) and their related changes during ozone pollution days in 2016 in Beijing. China. Environ Pollut 2020;257:113599.
[65] Platt U, Stutz J. Differential optical absorption spectroscopy. Berlin: Springer; 2008. p. 229–375.
[66] Altshuller AP. Production of aldehydes as primary emissions and from secondary atmospheric reactions of alkenes and alkanes during the night and early morning hours. Atmos Environ 1993;27(1):21–32.
[67] Seinfeld JH, Pandis SN. Atmospheric chemistry and physics: from air pollution to climate change. Hoboken: John Wiley & Sons; 2012.
[68] Schroeder JR, Crawford JH, Fried A, Walega J, Weinheimer A, Wisthaler A, et al. New insights into the column CH_2O/NO_2 ratio as an indicator of near-surface ozone sensitivity. J Geophys Res Atmos 2017;122(16):8885–907.
[69] Geng F, Tie X, Xu J, Zhou G, Peng Li, Gao W, et al. Characterizations of ozone, NO_x, and VOCs measured in Shanghai, China. Atmos Environ 2008;42(29):6873–83.
[70] Liu H, Liu C, Xie Z, Li Y, Huang X, Wang S, et al. A paradox for air pollution controlling in China revealed by "APEC Blue" and "Parade Blue". Sci Rep 2016;6(1):34408.
[71] Su W, Liu C, Hu Q, Fan G, Xie Z, Huang X, et al. Characterization of ozone in the lower troposphere during the 2016 G20 conference in Hangzhou. Sci Rep 2016;7(1):1–11.